



## Article

# The Impact of Internal Gravity Waves on the Spectra of Turbulent Fluctuations of Vertical Wind Velocity in the Stable Atmospheric Boundary Layer

Viktor A. Banakh \* and Igor N. Smalikho

V.E. Zuev Institute of Atmospheric Optics SB RAS, 1 Akademik Zuev Sq., Tomsk 634055, Russia; smalikho@iao.ru

\* Correspondence: banakh@iao.ru

**Abstract:** The wave turbulence interactions in the stable boundary layer (SBL) of the atmosphere are studied based on data from lidar measurements of the vertical component of wind velocity during the propagation of internal gravity waves (IGWs). It is shown that as an IGW appears, the amplitude of the spectra of turbulent fluctuations of vertical wind velocity nearby the frequency of quasi-harmonic oscillations induced by an IGW increases significantly, sometimes by several orders of magnitude, compared to the spectra in the absence of an IGW. Since IGW energy is transferred to small-scale turbulence, the amplitude of spectra with the Kolmogorov–Obukhov  $-5/3$  power-law frequency dependence in the inertial frequency range increases. The slope of the spectra in the low-frequency range between the frequency of IGW-induced oscillations and the frequency of the lower boundary of the inertial range exceeds the slope, corresponding to the  $-5/3$  power-law dependence. In this frequency range, the spectra obey the power-law dependence on the frequency with the exponent ranging from  $-4.2$  to  $-1.9$ . The average value of the exponent  $-3$  is consistent with a low-frequency slope caused by IGWs in turbulent spectra in the lower SBL.

**Keywords:** stable boundary layer; internal gravity wave; wind vertical velocity spectrum; wave turbulence interaction; coherent Doppler lidar



**Citation:** Banakh, V.A.; Smalikho, I.N. The Impact of Internal Gravity Waves on the Spectra of Turbulent Fluctuations of Vertical Wind Velocity in the Stable Atmospheric Boundary Layer. *Remote Sens.* **2023**, *15*, 2894. <https://doi.org/10.3390/rs15112894>

Academic Editors: Juan Luis Guerrero Rascado and Daniele Bortoli

Received: 28 April 2023

Revised: 28 May 2023

Accepted: 29 May 2023

Published: 1 June 2023



**Copyright:** © 2023 by the authors. Licensee MDPI, Basel, Switzerland. This article is an open access article distributed under the terms and conditions of the Creative Commons Attribution (CC BY) license (<https://creativecommons.org/licenses/by/4.0/>).

## 1. Introduction

The atmospheric boundary layer (ABL) significantly impacts the dynamics of the Earth's atmosphere. The exchange of energy, heat, and gases between the Earth's surface and the free atmosphere proceeds through the ABL. An important role in this process is played by wind turbulence, whose intensity depends, to a large extent, on the type of temperature stratification (unstable, neutral, or stable) [1–6]. Among these types, the hardest to describe is turbulence in the stably stratified atmosphere. At the stable stratification, turbulence does not always obey the Kolmogorov–Obukhov laws [7]. This necessitates the development of alternative theoretical approaches [8] and the extension of the experimental database on turbulence under these conditions. In the stable boundary layer (SBL) at the cooling of the Earth's surface [1–3,9], low-level jets (LLJs) with a maximum wind velocity at heights from 100 to 800 m are formed [4,9,10] and internal gravity waves (IGWs) arise, which may impact the small-scale wind turbulence by increasing velocity fluctuations in the inertial subrange. The processes of interaction of the wind turbulence and IGWs in the SBL should be taken into account in prognostic and climatic models [11]. The study of the wave turbulence interactions in the stably stratified atmosphere becomes increasingly urgent due to ongoing and accumulating global climate changes in recent decades [12].

According to the Kolmogorov–Obukhov theory [13,14], the energy spectra of wind velocity components in the inertial range of turbulence are characterized by the power-law frequency dependence  $f^\alpha$  with exponent  $\alpha = -5/3$ , and are proportional to  $\varepsilon^{2/3}$ , where  $\varepsilon$  is the turbulence kinetic energy (TKE) dissipation rate. At the stable stratification, the wind velocity spectra in the inertial frequency range can deviate from the  $-5/3$  power

dependence. The spectra behavior in the stably stratified surface layer of the atmosphere was analyzed thoroughly in [7]. It was shown in [7] that the exponent  $\alpha$  becomes larger than  $-5/3$  if the Richardson number  $Ri$  exceeds the level  $Ri = 0.2$  and takes the values at about  $-0.5$  at  $Ri = 2$  for all the wind velocity components. A part of the turbulence kinetic energy in a stably stratified atmosphere is expended on overcoming the buoyancy forces. As a result, the energy spectrum of the wind velocity components in the low-frequency range has power frequency dependence with the exponent  $\alpha$ , which is markedly smaller than  $-5/3$ . In particular,  $\alpha = -3$  [5,15] (Shur–Lumley equation) and  $\alpha = -11/5$  [5,16,17] (Bolgiano–Monin equation) were theoretically obtained. At present, a considerable number of works are devoted to the theoretical study and analysis of wavenumber spectra of wind velocity and temperature fluctuations observed in the upper troposphere and stratosphere [18–31]. The impact of internal gravity waves on the horizontal wavenumber spectra of velocity and temperature fluctuations in the upper troposphere and lower stratosphere is discussed in [5,19,22,23,27,32–34].

Aircraft experiments [20] show that in the range of horizontal scales from 500 km to several kilometers, the slope of the 1D horizontal wavenumber spectrum is determined by the exponent  $\alpha = -5/3$  of the power-law horizontal wavenumber dependence. At scales exceeding 500 km, the slope of the spectrum is determined by the exponent  $\alpha = -3$ . In aircraft measurements under stable atmospheric conditions, the power-law spectra of horizontal wind velocity and temperature fluctuations with the exponent ranging from  $-2.5$  to  $-3$  were observed at horizontal scales in the ranges of 15–23 km [35] and 0.3–6 km [5,18,22,32]. Collected aircraft data on turbulence in the lower 4 km stably stratified layer of the troposphere are analyzed in [36]. Observed vertical wavenumber spectra of the horizontal wind velocity and temperature fluctuations in the upper stratosphere have power-law vertical wavenumber dependence with the exponent  $\alpha$  equal to approximately  $-3$  in the range of vertical scales from several kilometers to tens of meters [37–41]. Following radiosonde observations [42], in the troposphere and lower stratosphere, the vertical wavenumber spectra of horizontal wind velocity fluctuations have power-law vertical wavenumber dependence, with a mean exponent  $\alpha = -2.6$  in the troposphere and  $\alpha = -2.9$  in the lower stratosphere. The slope of vertical wavenumber spectra of vertical wind velocity fluctuations differs significantly from the slope of vertical spectra of horizontal velocity. Power-law spectra of vertical velocity characterized by the exponent  $\alpha$  equals  $-0.58$  in the troposphere and  $-0.23$  in the lower stratosphere. The interaction between internal gravity waves and turbulence in the lower 300 m stably stratified nocturnal boundary layer is analyzed in [43]. Gravity waves and turbulence in the SBL are considered in [44] as well.

This paper reports the results of lidar studies of the IGW impact on the spectra of turbulent fluctuations of the vertical wind velocity in the stably stratified atmospheric boundary layer. Compared to other remote sensing methods and facilities (radars, sodars), coherent Doppler wind lidars provide higher spatial and temporal resolution of the measurement of velocity. That allows us to visualize the localization (in height and time) and dynamics of gravity wave evolution, from beginning to destruction and corresponding variations of the spectra of velocity fluctuations in more detail than can be performed using other remote sensing methods. Compared to mast measurements of the SBL, lidars provide measurements at higher altitudes. Seven hundred lidar estimates of the vertical wind velocity spectra obtained in experiments from 2020 to 2022 are analyzed to find the range of IGW-induced variations of the exponent of the power-law frequency dependence of the turbulence spectra.

## 2. Measurement Technique

To determine the wind velocity vector (time-averaged) and the spectra of turbulent fluctuations of the vertical velocity, we used a StreamLine (Halo Photonics, Brockham, Worcester, United Kingdom) pulse coherent Doppler lidar (PCDL) [45] and the measurement strategy proposed in [46]. First, one full scan around the vertical axis under an elevation angle  $\varphi = 60^\circ$  is performed for the time  $T_{\text{scan}} = 1$  min (see Figure 1 in [47]

illustrating scan geometry). Then, the beam is pointed vertically (elevation angle  $\varphi = 90^\circ$ ), and the vertical probing is conducted for the time  $T_{\text{vert}}$ . After that, the elevation angle is changed from  $90^\circ$  to  $60^\circ$  and the procedure is repeated. The duration of one measurement cycle is  $T_c = T_{\text{scan}} + \delta t + T_{\text{vert}} + \delta t$ , where  $\delta t \sim 10$  s is the time needed to change the elevation angle  $\varphi$ . In the experiment, the time of vertical probing was  $T_{\text{vert}} = 500$  s. The time for the measurement of the radial velocity  $\Delta t$  is determined by the number of laser shots used for the accumulation of raw data  $N_a$ , which is set equal to 7500. Assuming a pulse repetition rate of StreamLine PCDL  $f_p$  equal to 15 kHz (the main parameters of the StreamLine lidar can be found in Table 1 in [48]),  $\Delta t = N_a / f_p = 0.5$  s. Correspondingly, the number of measurements of the radial velocity was  $M_1 = T_{\text{vert}} / \Delta t = 1000$  per time  $T_{\text{vert}}$  and  $M_s = T_{\text{scan}} / \Delta t = 120$  per one scan.

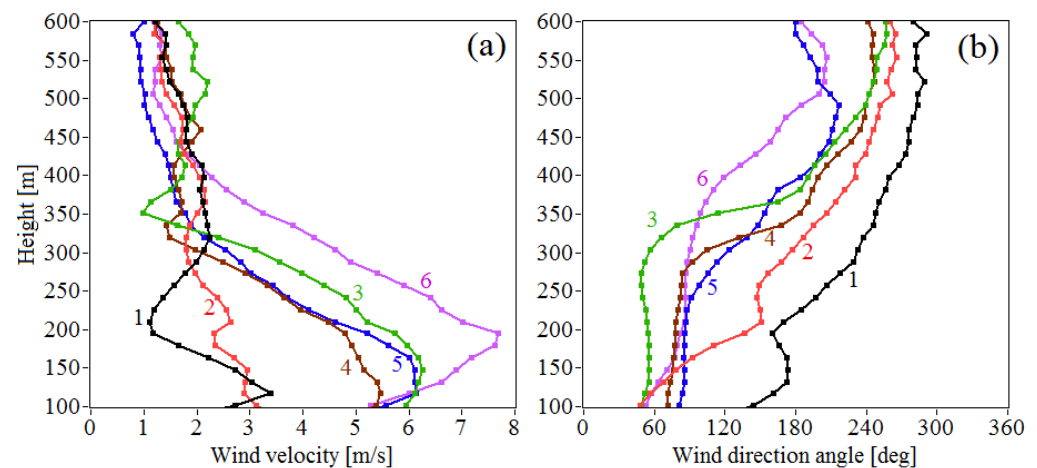


**Figure 1.** Vertical profiles of the horizontal wind velocity component  $U_1$  (a) and the wind direction angle  $\theta_V$  (b) calculated from lidar measurements at 03:06 (curves 1), 03:16 (curves 2), 03:26 (curves 3), 03:36 (curves 4), 03:46 (curves 5), and 03:56 (curves 6) of local time on July 6 of 2021. Each profile is drawn from measurement data obtained in one conical scan for 1 min.

As a result, we obtained two arrays of estimates of the signal-to-noise ratio  $\text{SNR}(m'\Delta t; R_k, \varphi_{\text{scan}}, n)$  and the radial velocity  $V_L(m'\Delta t; R_k, \varphi_{\text{scan}}, n)$  from measurements at the conical scanning and estimates of  $\text{SNR}(m\Delta t; R_k, \varphi_{\text{vert}}, n)$  and  $V_L(m\Delta t; R_k, \varphi_{\text{vert}}, n)$  from measurements in the vertical direction. Here,  $m' = 0, 1, 2, \dots, M_s - 1$ ;  $m = 0, 1, 2, \dots, M_1 - 1$ ;  $R_k = R_0 + k\Delta R$  is the distance from the lidar to the center of the probing volume;  $k = 0, 1, 2, \dots, K - 1$ ;  $\Delta R$  is the range gate length; and  $n = 1, 2, 3, \dots$  is the number of cycles of duration  $T_c$ . The azimuth resolution is  $\Delta\theta = 360^\circ / M_s = 3^\circ$ .

The sine wave fitting method [49] was applied to find the horizontal wind velocity  $U_1(h_k, n)$ , wind direction angle  $\theta_V(h_k, n)$ , and the velocity of the vertical wind component  $\bar{V}_z(h_k, n)$  averaged over the circle of the scanning cone base at the height  $h_k = R_k \sin \varphi_{\text{scan}}$  and over the time  $T_{\text{scan}}$  from the  $V_L(m'\Delta t; R_k, \varphi_{\text{scan}}, n)$  arrays. The  $V_L(m\Delta t; R_k, \varphi_{\text{vert}}, n)$  arrays were used to determine the vertical component of the wind velocity vector  $w$  and estimate the temporal  $S_L(f_l)$  and spatial  $S_L(\kappa_l)$  spectra of the vertical velocity, where  $f_l$  and  $\kappa_l = f_l / U$  are the frequencies and wavenumbers [50], respectively, and  $U$  is the mean horizontal velocity at the height of spectral measurements.

To obtain estimates of wind turbulence parameters, data measured for half an hour are usually used [9,51]. At  $T_{\text{vert}} = 500$  s, the cycle duration is  $T_c \approx 10$  min. Therefore, to estimate the spectrum of the vertical velocity measured by the lidar  $\hat{S}_L(f_l)$ , the data from three consecutive measurement cycles were used. Correspondingly, the mean velocity was estimated from four values of  $U_1$  as  $U(h_k, n) = (1/4) \sum_{i=0}^3 U_1(h_k, n - 1 + i)$ . The spectra  $S_L(f_l)$  are estimated from the arrays of the radial velocity  $V_L(m\Delta t; R_k, \varphi_{\text{vert}}, n)$  at heights  $h_k = R_k \sin \varphi_{\text{vert}} = R_k$ , which differ from the heights of estimation of the mean velocity

$h_k = R_k \sin \varphi_{\text{scan}}$ . To find the mean velocity at the height of spectra estimation, linear interpolation was applied.

Experimental temporal spectra of the vertical velocity  $S_L(f_l)$  were calculated as:

$$S_L(f_l) = \frac{1}{3} \sum_{i=0}^2 \frac{\Delta t}{M_1} \left| \sum_{m=0}^{M_1-1} V_L(m\Delta t; R_k, \varphi_{\text{vert}}, n-1+i) \exp\left(-2\pi j \frac{lm}{M_1}\right) \right|^2, \quad (1)$$

where  $f_l = l\Delta f$ ;  $l = 1, 2, 3, \dots, M_1/2$  is the number of the spectral channel;  $\Delta f = (M_1\Delta t)^{-1} = 0.002$  Hz is the width of the spectral channel; and  $0.002 \text{ Hz} \leq f_l \leq 1 \text{ Hz}$  and  $j = \sqrt{-1}$  are the imaginary units. A summation of spectral components over all the frequencies gives the estimate of the variance of vertical velocity:

$$\sigma_w^2 = 2\Delta f \sum_{l=1}^{M_1/2} S_L(f_l). \quad (2)$$

The Taylor hypothesis of frozen turbulence [50] allows us to pass from the temporal  $S_L(f_l)$  to spatial  $S_L(\kappa_l) = US_L(U\kappa_l)$  spectra, where  $\kappa_l = l\Delta\kappa$ ,  $\Delta\kappa = \Delta f/U$ . Whence, we can find  $S_L(f_l) = U^{-1}S_L(f_l/U)$  and  $\sigma_w^2 = 2\Delta\kappa \sum_{l=1}^{M_1/2} S_L(\kappa_l)$ .

The Taylor frozen turbulence hypothesis [50] can be applied within the frequency range from 0.05 to 0.2 Hz (except for the cases of very strong stability, this range falls within the inertial range of turbulence). Thus, using this hypothesis and the estimates of  $U$  and  $S_L(f_l)$ , we can find the dissipation rate  $\varepsilon$  by the algorithm described in [46]. The method proposed in [46] takes into account the effect of averaging the radial velocity over the probed volume and the noise component of the spectrum due to a random instrumental error in estimating the radial velocity. Below, in the figures for the spectra, the yellow curves show the theoretical spectra calculated by Formula (14) in [46], taking into account averaging over the probed volume and the noise and using the experimental value of the dissipation rate. The methods to determine the instrumental error of estimation of the radial velocity  $\sigma_e$  and the relative error of estimation of the dissipation rate  $E_\varepsilon$  are described in [46,52]. Using the method proposed in [48], we determined the amplitude  $A_z$  and frequency  $f_{\text{osc}}$  for the period  $T_{\text{osc}} = 1/f_{\text{osc}}$  of the IGW-induced quasi-harmonic oscillations of the vertical component of wind velocity.

To measure the temperature, we used the MTP-5 microwave temperature profiler (Atmospheric Technology, Dolgoprudnyi, Moscow, Russia) [53], which provided measurements of the vertical temperature profiles every 3 min with a resolution of 25 m for heights from 0 to 100 m and 50 m for heights from 100 to 1000 m. Thus, with the use of the profiler, we obtained the spatiotemporal distributions of the air temperature  $T(h, t)$  with a resolution time of 3 min and a height of 25–50 m for altitudes 0 to 1000 m above the ground. From these data, we calculated the potential temperature, vertical gradients of the potential temperature and, additionally using the wind data, the gradient Richardson number  $Ri$  [54].

### 3. Results of the Measurements

The measurements were conducted at the territory of the Basic Experimental Observatory (BEO) of the Institute of Atmospheric Optics (IAO) SB RAS in Tomsk, Russia (56°06′51.41″N, 85°06′03.22″E). The lidar was set on the ground, and the temperature profiler was installed at a height of 5 m above the ground. The continuous measurements were conducted from 28 June to 26 July 2020, from 1 July to 20 July 2021, and from 25 May to 30 May 2022.

In the experiments, the arrays of estimates of the radial velocity  $V_r(R_k, t_m) = V_L(t_0 + m\Delta t; R_k, \varphi_{\text{scan}}, n)$  and  $m = 0, 1, 2, \dots, M_s - 1$ , obtained by scanning, and  $V_r(R_k, t_m) = V_L(t_0 + m\Delta t; R_k, \varphi_{\text{vert}}, n)$  and  $m = 0, 1, 2, \dots, M_1 - 1$ , obtained at vertical probing, as well as the arrays of the corresponding SNR values  $\text{SNR}(R_k, t_m)$  as functions of the current

time  $t_m = t_0 + m\Delta t$  and the distance  $R_k = R_0 + k\Delta R$ ,  $k = 0, 1, 2, \dots, K-1$ , and  $\Delta R = 18$  m, were recorded. In the case of vertical probing, the elevation angle was  $\varphi_{\text{vert}} = 90^\circ$  and, correspondingly, the measurement height was  $h_k = R_k$  with the vertical step  $\Delta h = \Delta R$ . When analyzing the experimental results, we set  $h_0 = 99$  m and  $h_{K-1} = 621$  m relative to the lidar. Conical scanning with a probing beam was carried out at an elevation angle of  $\varphi_{\text{scan}} = 60^\circ$  and a measurement height of  $h'_k = R_k \cos 60^\circ$ .

Considering the time needed to change the elevation angle from  $90^\circ$  to  $60^\circ$  and back, the duration of one measurement cycle was  $T_c = 10$  min. By applying the sine wave fitting method to the arrays of estimates of the radial velocity measured at conical scanning, we obtained the estimates of the wind speed and direction for different heights as functions of time with the step  $T_c$ . From the height–time distributions of the vertical component of the wind velocity  $V_z(h_k, t_m) = V_r(R_k, t_m)$  at  $\varphi_{\text{vert}} = 90^\circ$ , we determined the time and duration of IGW propagation and assessed the spectra of the vertical velocity for these periods. Examples of the impact of the IGW on the spectra are considered below.

### 3.1. The IGW on 6 July 2021

On 6 July 2021, the IGW appeared after 03:00 local time (hereinafter, local time is indicated). As can be seen in Figure 1, LLJ with a maximum wind speed at a relatively low height begins to form at approximately the same time. This process is accompanied by a sharp change in the wind direction starting from a height of 300 m, which becomes the opposite above 500 m (Figure 1b).

Figure 2a shows the height–time distribution of the vertical component of wind velocity  $V_z(h_k, t_m)$ . The black color means no data since conical scanning by the probing beam was carried out at that time. Figure 2b shows the time series of the vertical velocity at different heights as obtained from the distribution in Figure 2a. The red circles in Figure 2b are for the estimates of the vertical velocity  $\bar{V}_z$  determined from conical scanning data. These estimates are in good agreement with the time series  $V_z(t_m)$  shown by the black curves in Figure 2b. It follows from Figure 2 that the IGW appeared at approximately 03:06 LT in the atmospheric layer of 100–600 m. This IGW caused oscillations of the vertical velocity with an amplitude  $A_z$  up to 1 m/s (at a height of 405 m) in the initial period.

Within an hour, the amplitude  $A_z$  gradually decreased, while the period of oscillations  $T_{\text{osc}}$  increased by almost 1.5 times. At heights of 405 and 513 m, where the wind turbulence is weak, variations of the vertical velocity have the form of quasi-harmonic oscillations. Uncorrelated random dribbling of the time series  $V_z(t_m)$  at these heights is associated with instrumental error, which increases with height due to a decrease in the SNR. In the low layers (in particular, at heights of 297 and 207 m), random deviations of  $V_z(t_m)$  due to wind turbulence are quite significant and lead to a distortion of the quasi-harmonic form of wind velocity oscillations.

Figure 3a shows the time series of the vertical component of wind velocity  $V_z(t_m)$  at a height of 405 m in the period from 02:00 to 06:00 LT. One can see that the IGW that appeared at 03:06 decayed gradually over almost two hours until IGW energy was completely converted into the energy of turbulent wind velocity variations.

To determine the frequency  $f_{\text{osc}}$  of quasi-harmonic oscillations of wind velocity (oscillation period  $T_{\text{osc}} = f_{\text{osc}}^{-1}$ ) induced by IGW propagation, we used the data in Figure 3a at non-overlapping time intervals of 03:06–03:26 and 03:26–03:46 LT shown in Figure 3a by the blue and red arrows, respectively. From the data for  $V_z(t_m)$  at these intervals, after uniform interpolation and the addition of the corresponding number of zeros to each of the velocity arrays, we obtained two power spectra of vertical velocity variations. These spectra are shown in Figure 3b. From the position of the maximum of each of these spectra (see the brown vertical lines in Figure 3b), we found that the frequency was  $f_{\text{osc}} = 0.0021$  Hz (period  $T_{\text{osc}} \approx 8$  min) in the interval of 03:06–03:26 and  $f_{\text{osc}} = 0.0015$  Hz (period  $T_{\text{osc}} \approx 11$  min) in the interval of 03:26–03:46.



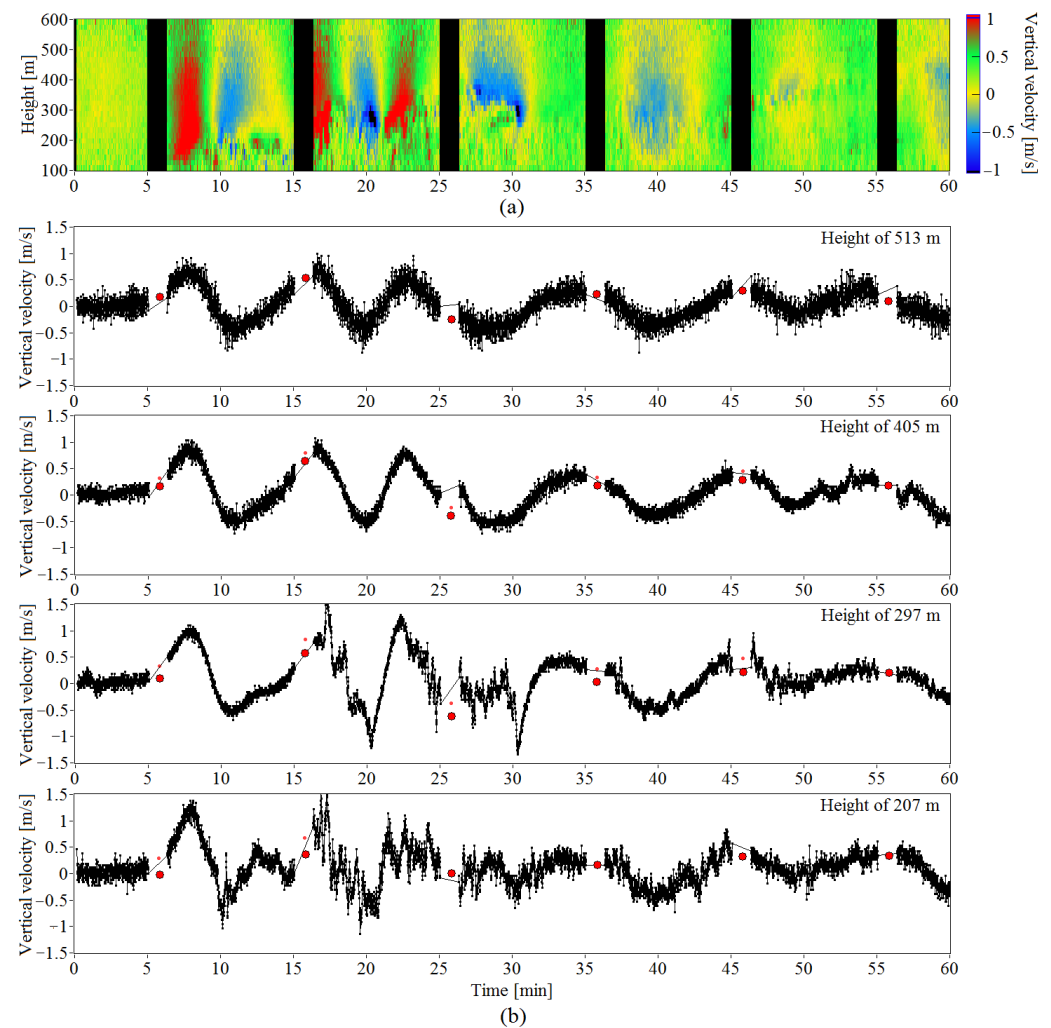


**Figure 2.** Height–time distribution of the vertical component of the wind velocity vector (a) and time series of the vertical component of the wind velocity vector at heights of 207, 297, 405, and 513 m (b). The red circles in (b) are for the estimates of the vertical velocity  $\bar{V}_z$  determined from conical scanning data. Measurements within an hour starting from 03:00 LT on 6 July 2021.

The only parameter characterizing the spectra of the turbulent field of velocities in the inertial frequency range is the TKE dissipation rate  $\epsilon$ . The larger the SNR, the smaller the error of  $\epsilon$  estimation from lidar velocity measurements. To minimize the errors in estimating the spectra of turbulent fluctuations of the vertical velocity, we used the data in Figure 2b for the time series  $V_z(t_m)$  at a height of 297 m. This height nearly coincides with a height of 300 m, at which the SNR is maximal as follows from the height–time distribution of the  $\text{SNR}(h_k, t_m)$  obtained from the measurements by the StreamLine lidar on 6 July 2021. A height of 300 m corresponds to the distance that the probing beam was focused at. Thus, the instrumental error  $\sigma_e$  of estimation of the vertical wind velocity  $V_z(t_m)$  and, consequently, the relative errors of estimation of the dissipation rate and the spectrum are minimal. The spectra  $S_L(f_l)$  were calculated by Equation (1) for four 30 min intervals, whose boundaries are shown by the black arrows in Figure 3a. The results are shown as black curves in Figure 4.

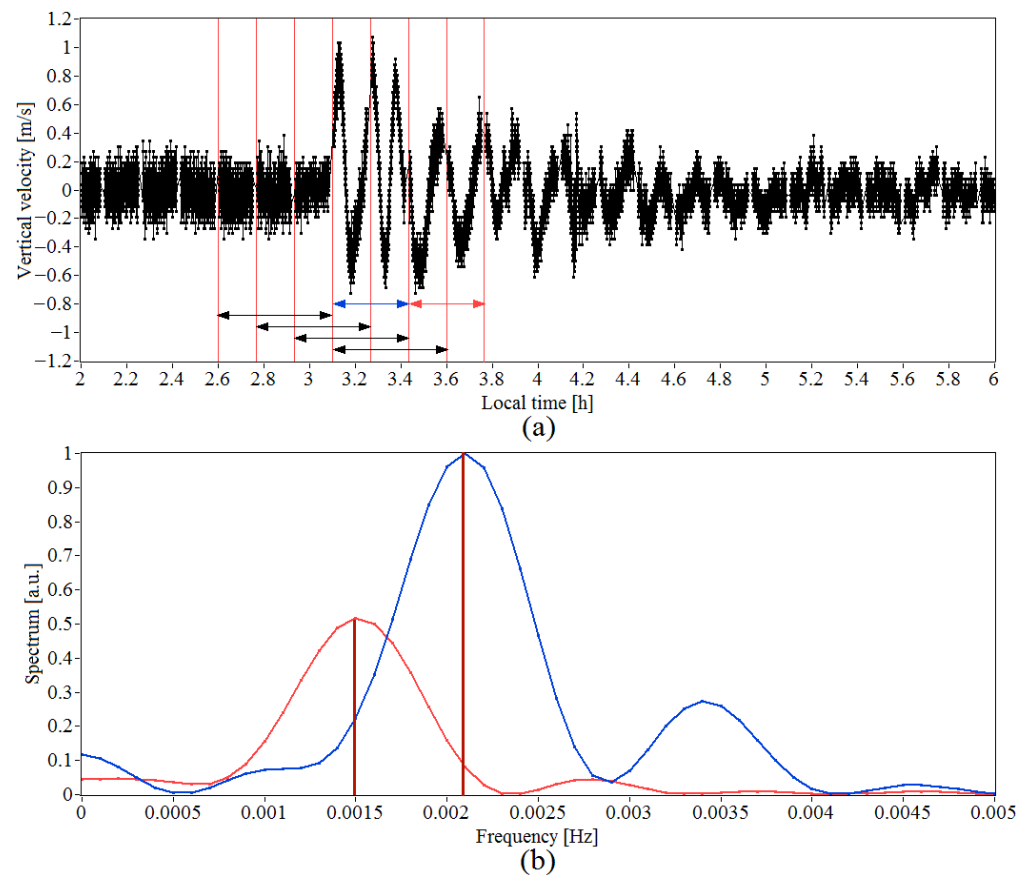


**Figure 3.** Time series (a) and power spectra of the vertical component of wind velocity at time intervals of 03:06–03:26 LT (blue arrow, blue curve) and 03:26–03:46 LT (red arrow, red curve) (b) at a height of 405 m. Black arrows in (a) show time intervals for which the spectra in Figure 4 calculated. Measurements were taken on 6 July 2021.

As in Figure 3a, the vertical brown lines in Figure 4 show the frequencies  $f_{\text{osc}}$  of IGW-induced velocity oscillations determined in the same way as described above. There is no such line in the spectrum calculated for the first interval of 02:36–03:06 because the IGW has not yet appeared at that time. The spectra within the frequency  $f_l$  range from 0.05 to 0.2 Hz (shown by the red arrows in Figure 4) were used to estimate the TKE dissipation rate  $\varepsilon$  by the method proposed in [46]. It can be seen that as the IGW appears, the spectral amplitude nearby the frequency  $f_{\text{osc}}$  increases by more than two orders of magnitude. As a consequence, the variance of the vertical wind velocity  $\sigma_w^2$  calculated by Equation (2) as a sum of amplitudes at frequencies  $f_l \geq 0.002$  Hz increases as well. The lower boundary  $f_l = 0.05$  Hz of the frequency range, within which the dissipation rate is determined, is far higher than  $f_{\text{osc}}$  (approximately 25 times higher). Nevertheless, the IGW also leads to an increase in the dissipation rate  $\varepsilon$ . An increase in the spectrum amplitude by an order of magnitude within the turbulence inertial range (purple lines) is clearly seen in the two lower figures compared to the upper figures in Figure 4. This is likely due to the partial transfer of IGW energy to small-scale turbulent variations of the vertical component of wind velocity.

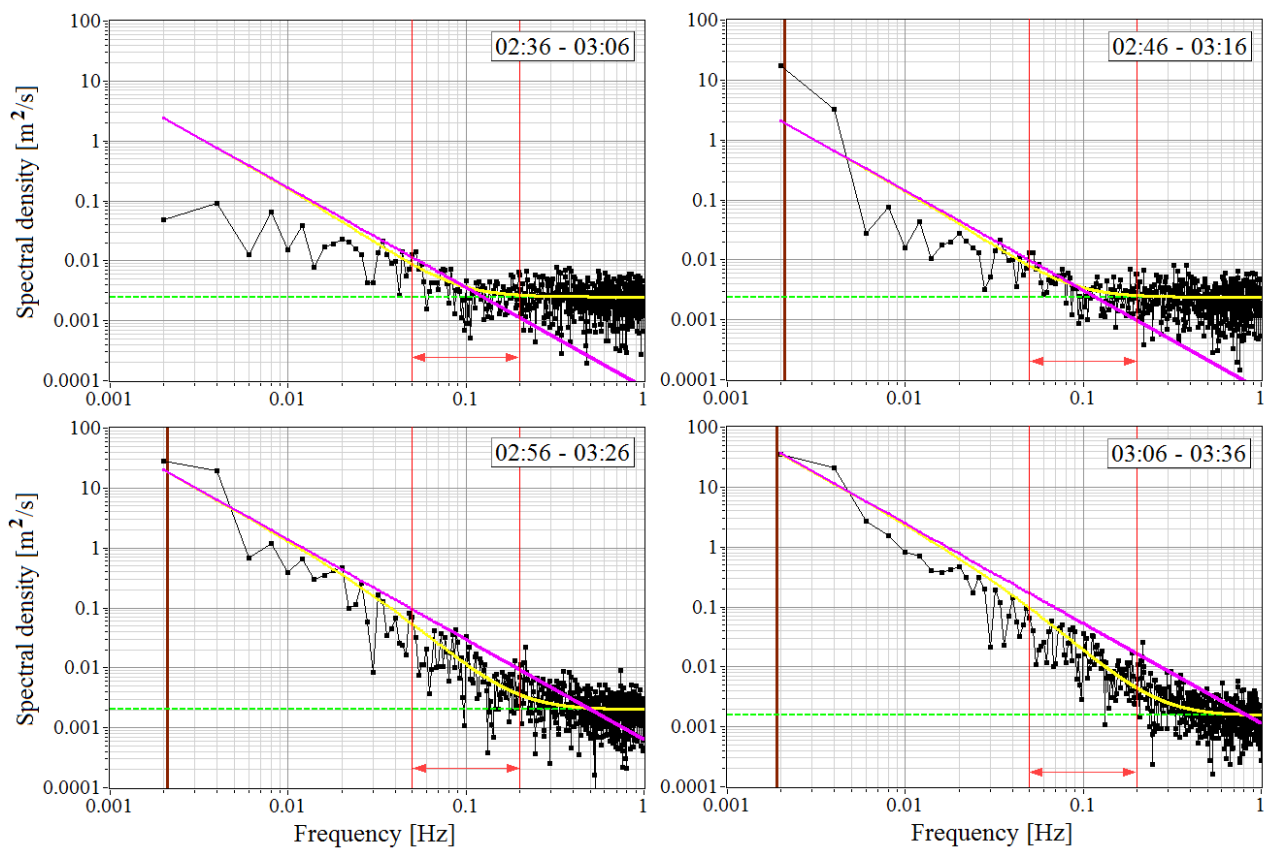


**Figure 4.** Spectra of the vertical component of the wind velocity vector at a height of 297 m calculated for the measurement intervals shown by the black arrows in Figure 3a (black curves). Green dashed lines show the noise component of the spectrum. Red arrows show the interval, within which the turbulent energy dissipation rate  $\varepsilon$  is determined by our method described in [46]. Yellow curves are for the theoretical spectra calculated by us using Equation (14) in [46] and the experimental values of  $\varepsilon$ . The purple lines are for the  $-5/3$  Kolmogorov–Obukhov spectra calculated by us using Equation (18) in [46]. The brown vertical lines show the frequencies of IGW-induced quasi-harmonic oscillations of the vertical velocity. Measurements were taken on 6 July 2021.

Figure 5 shows the height–time distributions of the instrumental error of estimation of the radial velocity  $\sigma_e(h_k, t_n)$ , the variance of the vertical wind velocity  $\sigma_w^2(h_k, t_n)$ , the TKE dissipation rate  $\varepsilon(h_k, t_n)$ , and the relative error of estimation of the dissipation rate  $E_\varepsilon(h_k, t_n)$  with a height step of 18 m and a time step of 10 min. These distributions were obtained from measurements by StreamLine lidar from 00:00 to 12:00 LT on 6 July 2021. The black color in Figure 5d means that  $E_\varepsilon(h_k, t_n)$  exceeds the level of 50%. The white rectangles show the boundaries of the height–time domain, in which the IGW was observed. One can see that the dissipation rate  $\varepsilon$  and the variance of the vertical velocity  $\sigma_w^2$  that characterize the intensity of wind turbulence have larger values in this domain than outside it.



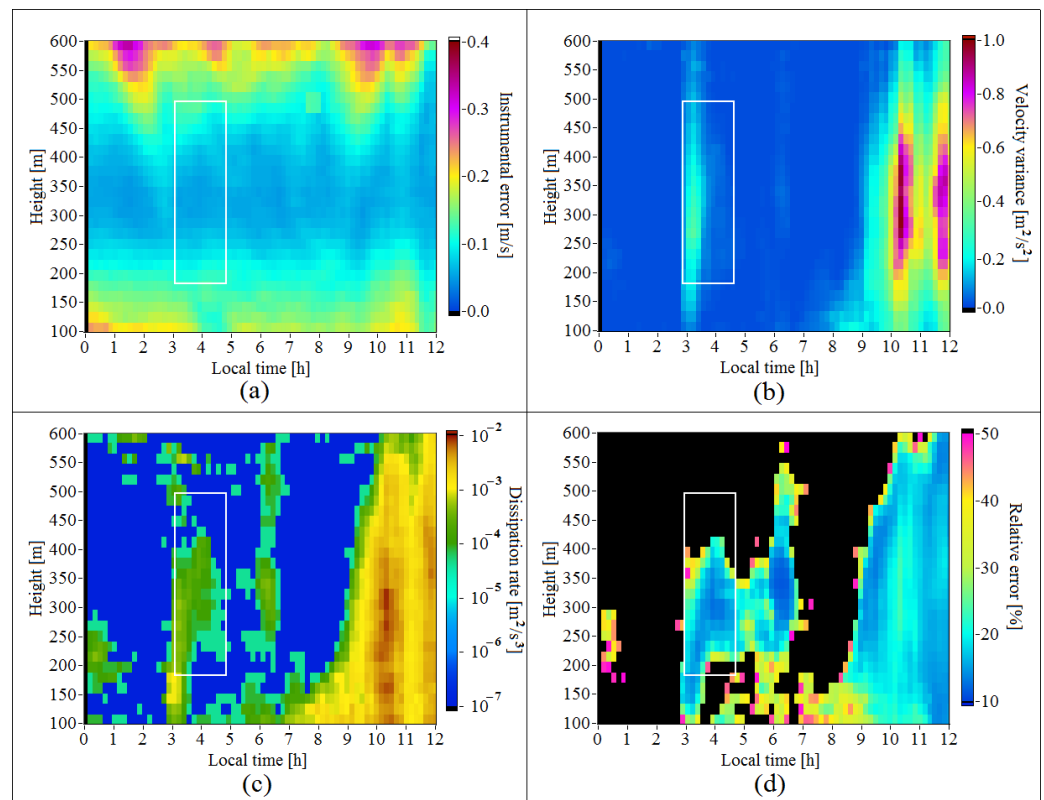


**Figure 5.** Height–time distributions of the instrumental error of estimation of the radial velocity (a), the variance of the vertical component of the wind velocity vector (b), turbulent kinetic energy (TKE) dissipation rate (c), and the relative error of estimation of the dissipation rate (d) on 6 July 2021. The white rectangle bounds the height–time domain of the IGW observation.

### 3.2. The IGW on 28 May 2022

On 28 May 2022, the IGW emerged during a rather strong low-level jet at 02:30 and lasted until 05:30 LT. Figure 6 shows the vertical profiles of the horizontal wind velocity obtained in this interval. It can be seen that the height of the maximum velocity (LLJ center) decreased from 350 to 240 m in 2.5 h. The IGW was observed only in the top part of the jet, while below the center of the LLJ, there was quite intense turbulent air mixing.

The height–time distribution of the vertical wind velocity in the period from 02:00 to 05:00 LT on 28 May 2022 is shown in Figure 7a. As in Figure 2a, the black color shows the time intervals, in which conical scanning by the probing beam was carried out to determine the wind speed  $U_1$  and the wind direction angle  $\theta_V$ . In Figure 7a, we can see oscillations of the vertical velocity at heights from 250 to 450 m that are caused by the IGW propagating in this layer. Below 250 m, turbulent velocity fluctuations that are quite intense for the nighttime are observed. Figure 7b shows the time series of the vertical wind velocity at a height of 351 m drawn from the data in Figure 7a. It follows from Figure 7b that the amplitude of quasi-harmonic oscillations of the vertical velocity does not exceed 0.8 m/s.

After applying low-pass filtering and spline interpolation of data with a uniform rather small time step to the time series shown in Figure 7b and dividing it into six 30 min intervals, we calculated the temporal spectra for each interval. The positions of maxima in these spectra were used to determine the frequencies  $f_{\text{osc}}$  and calculate the periods  $T_{\text{osc}} = 1/f_{\text{osc}}$  of quasi-harmonic oscillations of the vertical velocity. Figure 7c shows how the oscillation period changed during IGW passage. It can be seen that  $T_{\text{osc}}$  decreased with time from approximately 6 min down to almost 1 min.

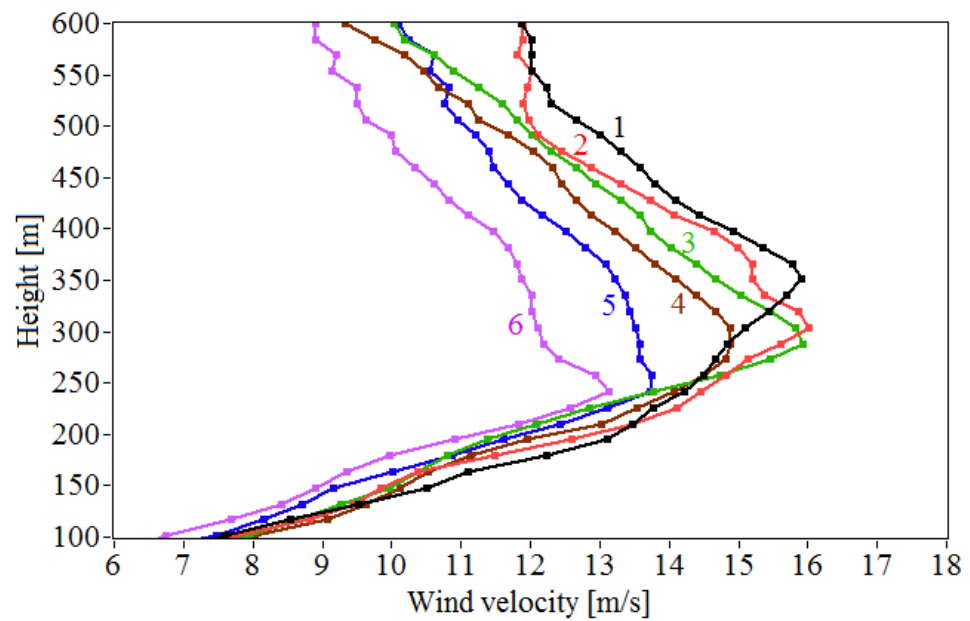


**Figure 6.** Vertical profiles of the horizontal component of wind velocity  $U_1$  obtained from lidar measurements at 02:32 (1), 03:02 (2), 03:32 (3), 04:02 (4), 04:32 (5), and 05:02 (6) LT on 28 May 2022.

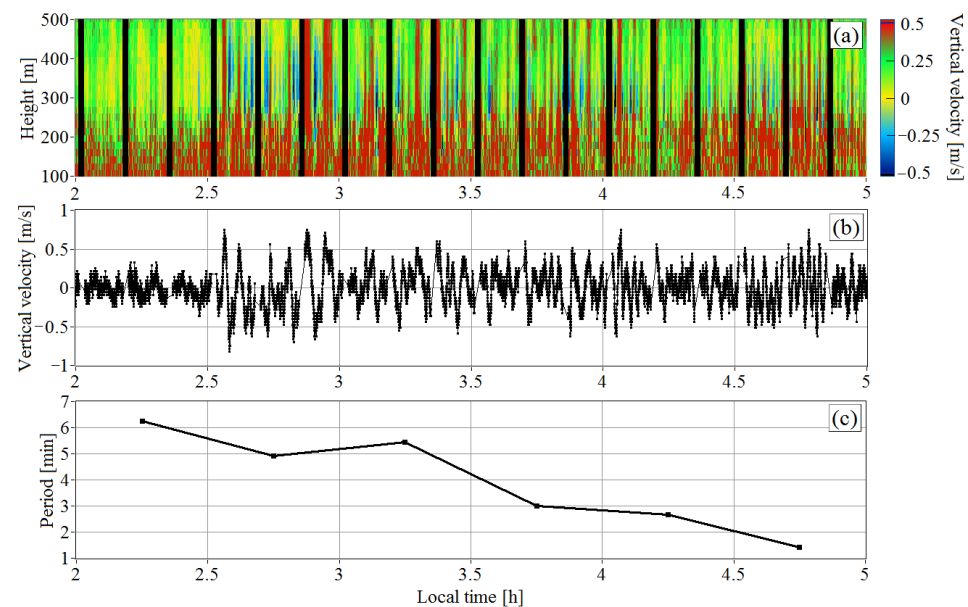


**Figure 7.** Height–time distribution (a), time series at a height of 351 m (b), and period of quasi-harmonic oscillations of the vertical velocity as a function of time (c) obtained from lidar measurements on 28 May 2022.

Using the data in Figure 7b, we calculated the spectra of turbulent fluctuations of vertical velocity  $S_L(f_l)$  for different time intervals. Three of these spectra are shown in Figure 8. The brown vertical lines show the frequencies of oscillation  $f_{osc}$  corresponding to the periods  $T_{osc} = 1/f_{osc}$  in Figure 7c. We can see that the frequency  $f_{osc}$  increases with time (compare (a), (b) and (c) in Figure 8 between themselves). The IGW leads to an increase in the amplitude of the spectrum  $S_L(f_l)$  in the frequency range from  $f_{osc}$  to 0.05 Hz. Thus, the slope of the spectrum in this range becomes larger than the slope of the spectrum with the  $-5/3$  power-law frequency dependence  $\sim f_l^{-5/3}$ .

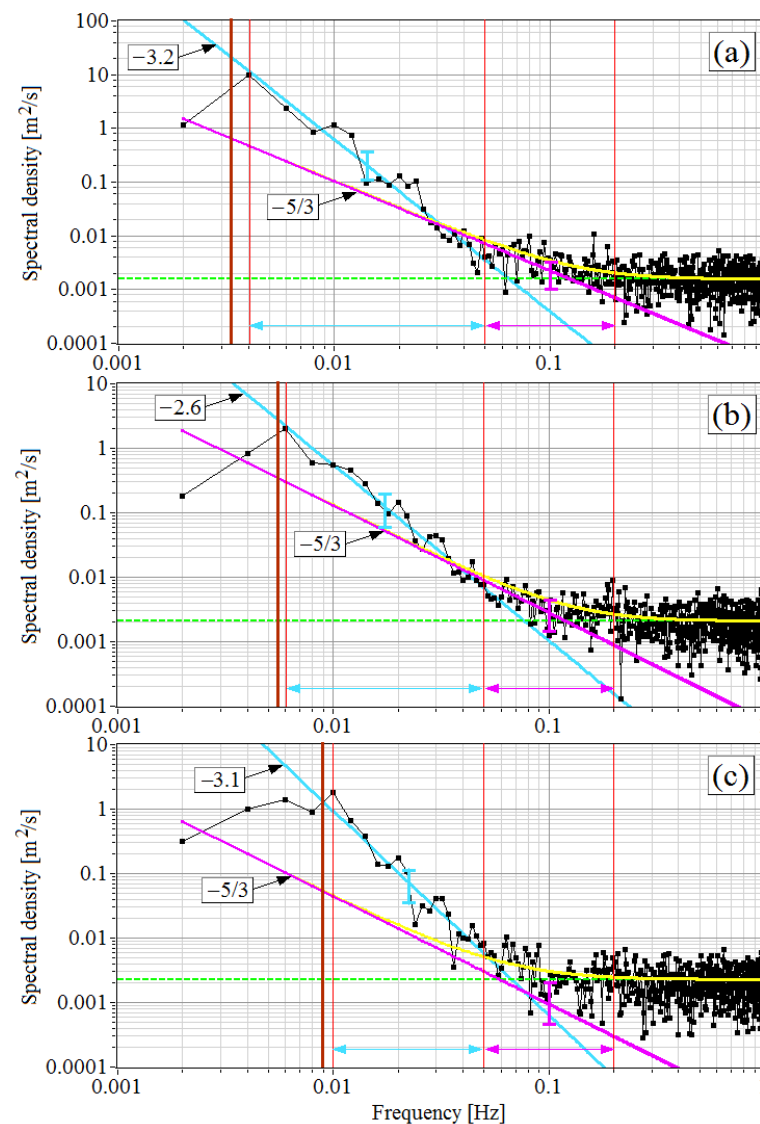


**Figure 8.** Spectra of the vertical component of wind velocity (the black curves with squares) obtained from lidar measurements on 28 May 2022 from 02:30 to 03:00 (a), from 03:30 to 04:00 (b), and from 03:50 to 04:20 LT (c) at a height of 351 m. Noise spectral components are shown by the green dashed lines. The purple arrows indicate the interval, within which the TKE dissipation rate  $\varepsilon$  was estimated by the method described by us in [46]. The obtained values of the dissipation rate were used by us to calculate the theoretical spectra using Equation (14) in [46], with allowance for noise and averaging over the probing volume (yellow curves) and the  $-5/3$  frequency dependence (purple lines). The brown vertical lines show the frequencies of quasi-harmonic oscillations of the vertical velocity. The blue lines are the results of fitting the power-law dependence to the experimental spectra in the intervals indicated by the blue arrows. For the pink and blue curves, 95 percent confidence intervals are indicated.

To characterize the spectra in the frequency range from  $f_{\text{osc}}$  to 0.05 Hz, we assume that the spectra of the vertical velocity averaged over an ensemble of realizations  $\langle S_L(f_l) \rangle$  are characterized by power-law dependence  $\langle S_L(f_l) \rangle = A f_l^\alpha$ , where  $A$  is the frequency-independent coefficient and  $\alpha$  is the exponent. Then, through the least-square fitting of the linear dependence  $\lg A + \alpha \lg f_l$  on  $\lg f_l$  to  $\lg(S_L(f_l))$  within this interval, we find  $A$  and  $\alpha$  and approximate the experimental spectra by the power-law frequency dependence. In Figure 8, the obtained frequency functions  $A f_l^\alpha$  are shown by blue lines with an indication of the exponent:  $\alpha = -3.2$  (Figure 8a),  $\alpha = -2.6$  (Figure 8b), and  $\alpha = -3.1$  (Figure 8c). These

estimates of  $\alpha$  differ significantly from  $-5/3$  and are relatively close to the Lumley–Shur theoretical value  $\alpha = -3$  and the  $-3$  frequency dependence in the low-frequency range of the turbulent spectra in the SBL [43].

The same method was used to estimate the exponent  $\alpha$  of the spectrum in the frequency range of 0.006–0.05 Hz for the time interval from 00:00 to 08:00 LT on 28 May 2022 with a 10 min step from lidar measurements at a height of 351 m. The obtained time series  $\alpha(t)$  is shown as a black curve in Figure 9a. The time series of the Richardson number calculated from the lidar data on the wind velocity and from the temperature profiler data with the same time step is shown in Figure 9b. It follows from Figure 9b that the temperature stratification was stable at a height of 351 m in the considered period, and the Richardson number was  $Ri > 0$ . According to the temperature data, stable stratification in the boundary layer above 200 m was observed starting from 20:00 LT on May 27. It can be seen in Figure 9b that before the IGW appeared at 02:30 and after IGW destruction, starting from 05:00 LT, the Richardson number exceeded the values of  $Ri$  observed during IGW propagation from 02:30 to 05:00 LT by one to two orders of magnitude. In Figure 9a, we can see that before and after the IGW, the exponent  $\alpha$  exceeds  $-5/3$  and ranges approximately within  $-0.7 > \alpha > -1.5$ . This is consistent with the variability range of the slopes of the temporal spectra of wind velocity components observed during stable stratification in the atmospheric surface layer in the Arctic [7]. During IGW propagation from 02:30 to 05:00 LT, the exponent  $\alpha$  becomes less than  $-5/3$  and falls in the range of  $-2.5 > \alpha > -3.5$ . During IGW passage,  $\alpha$  averages  $-3$ .

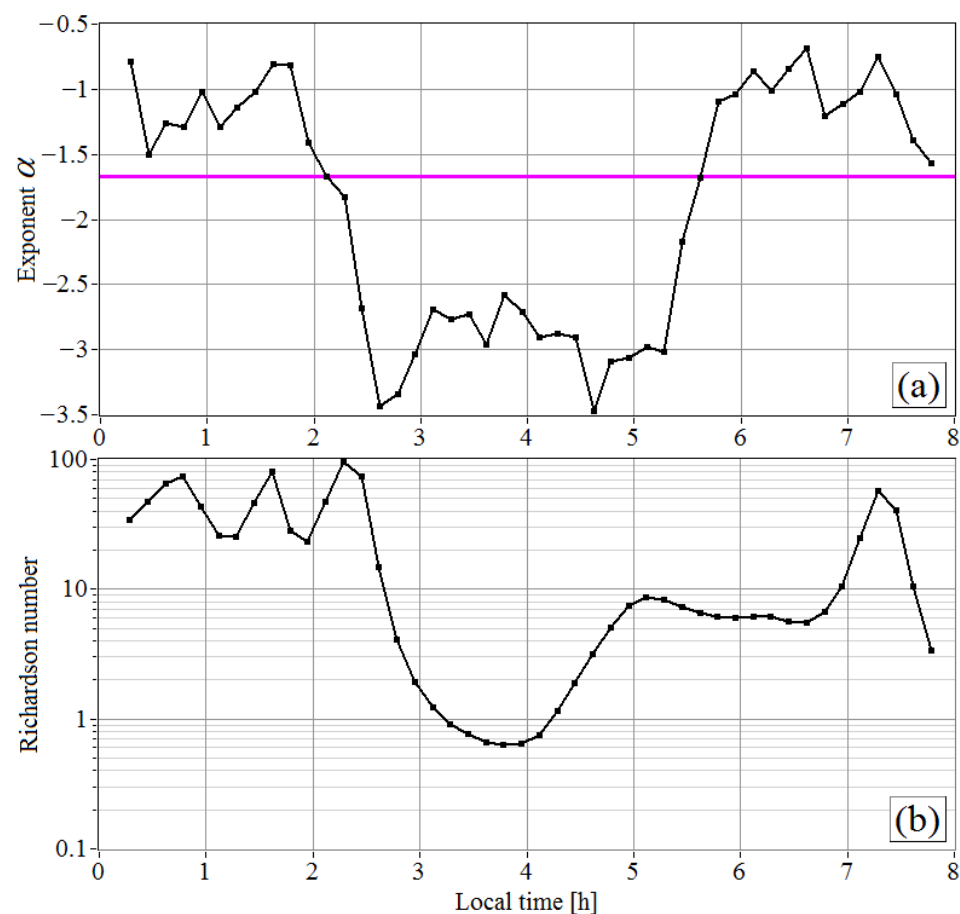


**Figure 9.** Time series of the exponent  $\alpha$  determined from the fitting of the power dependence to the experimental spectra of vertical wind velocity in the frequency range from 0.006 to 0.05 Hz (a) and the Richardson number (b) (black curves). The data of measurements by the StreamLine lidar and MTP-5 microwave temperature profiler on 28 May 2022 at a height of 351 m are used. The purple line corresponds to the exponent of  $-5/3$ .

Figure 10 shows the height–time distributions of  $\sigma_e(h_k, t_n)$ ,  $\sigma_w^2(h_k, t_n)$ ,  $\varepsilon(h_k, t_n)$ , and  $E_\varepsilon(h_k, t_n)$  obtained from 24 h lidar measurements on 28 May 2022. The white rectangle bounds the domain of IGW observation. It can be seen that for most of this domain, the relative error in estimating the TKE dissipation rate does not exceed 30%. The dissipation rate in this domain varies from  $10^{-7} \text{ m}^2/\text{s}^3$  to  $5 \cdot 10^{-4} \text{ m}^2/\text{s}^3$ , and it does not exceed  $10^{-5} \text{ m}^2/\text{s}^3$  in 75% of cases and  $10^{-6} \text{ m}^2/\text{s}^3$  in 50% of cases.

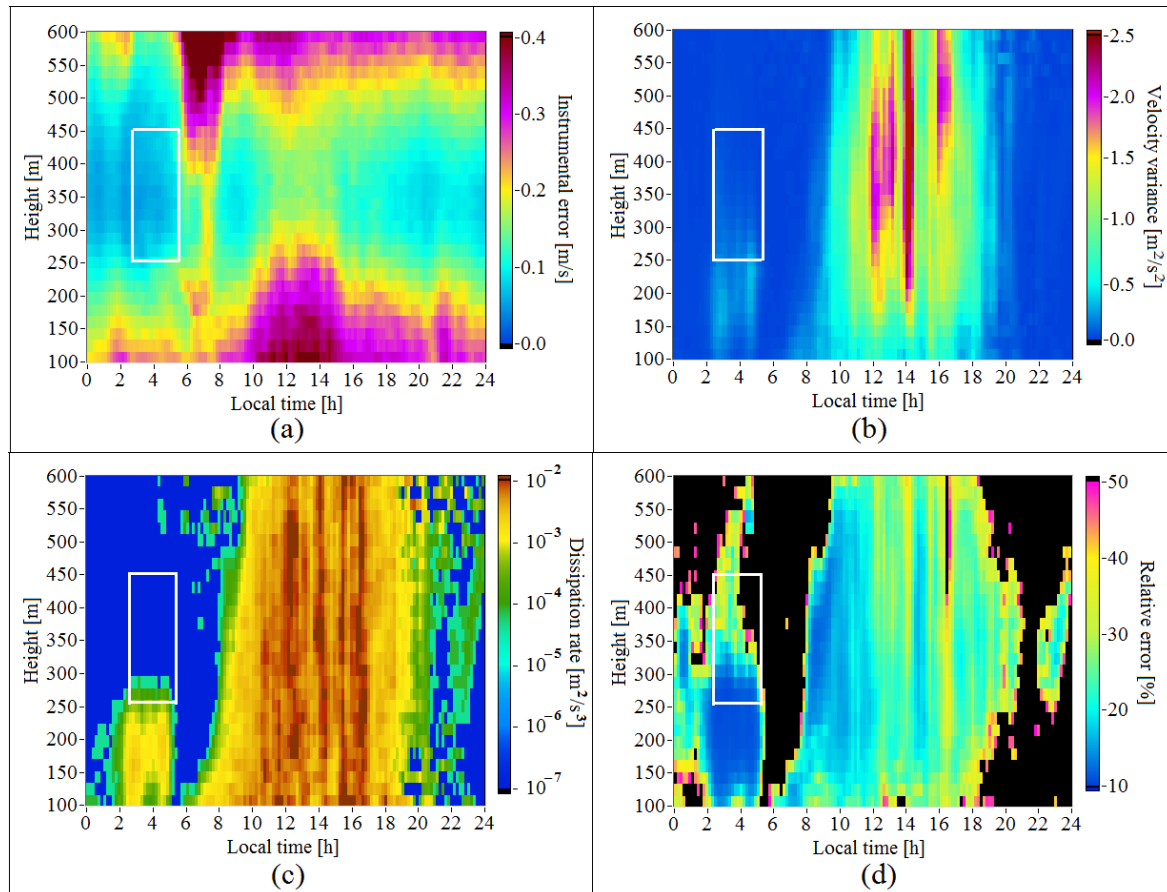


**Figure 10.** Height–time distributions of the instrumental error of estimation of the radial velocity (a), the variance of the vertical component of the wind velocity vector (b), TKE dissipation rate (c), and relative error of estimation of the dissipation rate (d). The white rectangle bounds the domain of IGW observation. Measurements were taken on 28 May 2022.

### 3.3. The IGW on 30 May 2022

On 30 May 2022, the IGW was observed in the period from 04:00 to 07:40 LT. Figure 11 depicts the spectra of the vertical wind velocity component obtained from lidar measurements at different heights during the propagation of the IGW with  $f_{\text{osc}} \approx 0.003 \text{ Hz}$  in the atmospheric layer of 250–600 m. To avoid the influence of the noise spectral component  $S_L(f_l)$ , we determined the exponent  $\alpha$  within the frequency range from 0.004 to 0.02 Hz. The figure clearly illustrates the significant excess of the spectrum slope (blue lines) over the  $-5/3$  slope (purple lines) for heights starting from 297 m.

Figure 12 depicts the vertical profiles of the horizontal wind velocity  $U(h_k)$ , TKE dissipation rate  $\varepsilon(h_k)$ , relative error of lidar estimation of the dissipation rate  $E_\varepsilon(h_k)$ , exponent  $\alpha(h_k)$ , temperature  $T(h_k)$ , and Richardson number  $Ri(h_k)$ . It follows from Figure 12e,f that during the measurements at heights of 100–600 m, the temperature stratification in the boundary layer is stable, the temperature  $T(h_k)$  increases with height, and the Richardson number is positive  $Ri(h_k) > 0$ . In the height range of 100–250 m, where the IGW effect is insignificant,  $Ri(h_k)$  does not exceed unity, and the exponent  $\alpha(h_k) > -5/3$ . The range of



exponent variation at heights of 100–250 m is  $-0.2 > \alpha(h_k) > -5/3$ , which is consistent with the values of  $\alpha$  in Figure 9a in the absence of the IGW. Starting from a height of 250 m, where the IGW effect is already noticeable,  $Ri(h_k)$  increases fast and achieves 300 at heights of 400–500 m, where the IGW effect is maximal (see Figure 11). Simultaneously, the exponent  $\alpha$  decreases sharply starting from a height of 250 m. At heights of 400–550 m, where the IGW energy is maximal, the exponent is  $\alpha \approx -3$ .

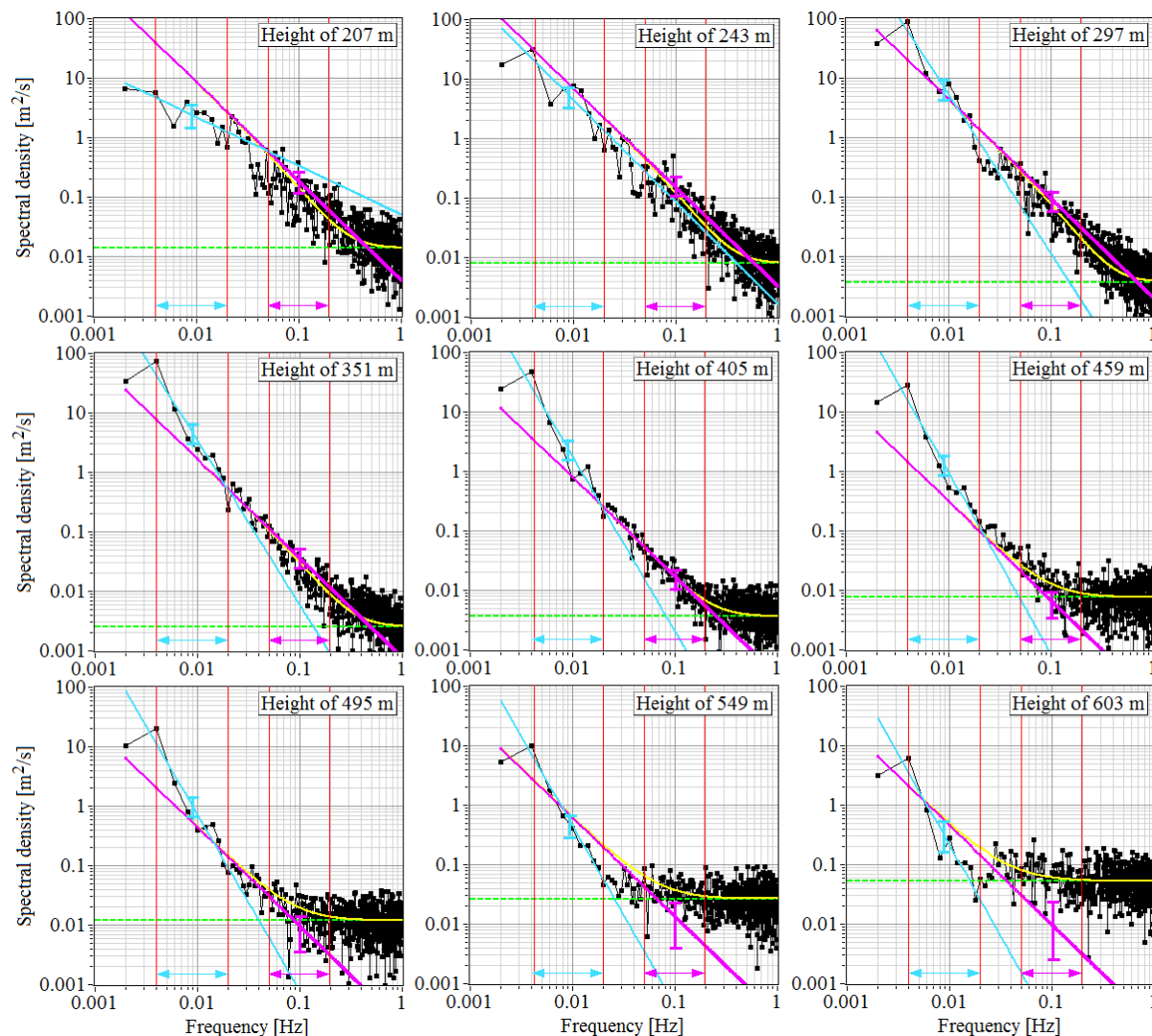


**Figure 11.** Spectra of the vertical component of wind velocity (black curves with squares) obtained from lidar measurements on 30 May 2022, from 06:04 to 06:34 LT, at different heights. Noise components of the spectra are shown by green dashed lines. The purple arrows show the range, within which the TKE dissipation rate  $\varepsilon$  was estimated by the method described by us in [46]. The obtained values of the dissipation rate were used to calculate the theoretical spectra using Equation (14) in [46] with allowance for noise and averaging over the probing volume (yellow curves) and the  $-5/3$  frequency dependence of the spectrum (purple lines). The blue lines are the results of fitting the power-law dependence to the experimental spectra in the intervals indicated by the blue arrows. For the pink and blue curves, 95 percent confidence intervals are indicated.

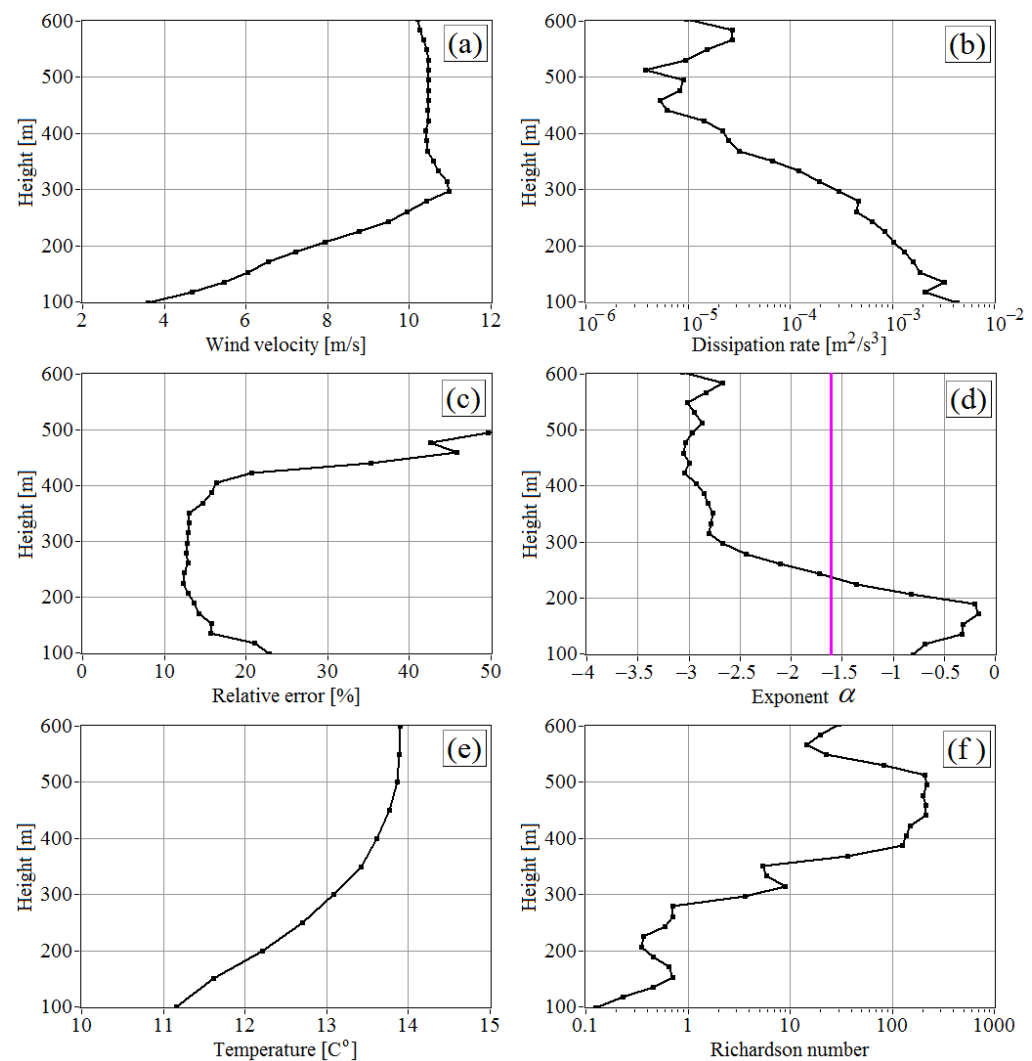


**Figure 12.** Vertical profiles of the horizontal wind velocity (a), TKE dissipation rate (b), the relative error of lidar estimation of the dissipation rate (c), exponent calculated by fitting the power-law dependence to the experimental spectra of the vertical wind velocity in the frequency range from 0.004 to 0.02 Hz (d), mean air temperature (e), and Richardson number (f). The purple line corresponds to the exponent of  $-5/3$ . The measurement data of the StreamLine lidar and the MTP-5 microwave temperature profiler from 06:04 to 06:34 LT on 30 May 2022 were used.

#### 4. Discussion

The continuous lidar measurements were conducted in different periods from May to July of 2020, 2021, and 2022 within 53 days in total. During this time, we observed 23 events of IGW that arose at night and in the morning (from 02:00 to 08:00 local time). In approximately half of the events, the duration of IGW-induced continuous quasi-harmonic oscillations of the vertical velocity ranged from 0.5 to 5 h. The total duration of their observation was 25 h. The waves were observed in a stably stratified ABL at heights from 200 to 600 m.

In the overwhelming majority of cases, IGWs in a stably stratified boundary layer occur during LLJs. The ratio of the total duration of the LLJ observed during the measurements to the total lifetime of the IGW that occurred during the LLJ is approximately 4.3. During the measurements, only two cases of IGW formation in the absence of a jet were revealed. This happened when the wind speed did not exceed 3 m/s, and the wind direction alternated sharply to the opposite direction with height. We can assume that the vertical inhomogeneity of wind in the velocity (LLJ) or direction is one of the reasons for IGW generation in the SBL.

Using the results of lidar measurements during the propagation of IGWs in the atmospheric boundary layer, we calculated 700 spectra of the vertical component of the wind velocity  $S_L(f_l)$ : 220 spectra from measurements in 2020, 155 spectra from measurements in 2021, and 325 spectra from measurements in 2022. The spectra were calculated for the periods of IGW propagation, with a time step of 15 min and a height step of 18 m in an altitude range from 200 to 600 m.

All the spectra  $S_L(f_l)$  were estimated from 30 min measurements of the vertical wind velocity  $V_z(h_k, t_m)$  under the following conditions: (1) the IGW observed during the entire 30 min measurement interval, (2) the height  $h_k$  not below the LLJ center (height of the maximal horizontal wind velocity  $U(h_k)$ ), (3) IGW frequency  $f_{osc}$  not higher than 0.02 Hz, (4) the SNR not lower than  $-18$  dB, (5) and stable temperature stratification.

For each spectrum, the exponent  $\alpha$  was calculated assuming the power-law dependence on frequency in the low-frequency region. When determining  $\alpha$  from the selected spectra  $S_L(f_l)$ , we set the upper boundary of the frequency range, within which  $\alpha$  was estimated, depending on the level of the noise component of the spectrum (not lower than 0.02 Hz and not higher than 0.06 Hz). The lower boundary of the frequency range was taken to be not lower than the frequency of IGW-induced oscillations of the vertical velocity  $f_{osc}$ . Figure 13 shows the histogram of all the obtained estimates of  $\alpha$ . It follows from the data in Figure 13 that the average value of the exponent is  $\langle \alpha \rangle = -3$ , while the standard deviation of the estimates is 0.44. The probability that the estimate of the exponent  $\alpha$  takes a value from  $-3.5$  to  $-2.5$  is 80%. The obtained estimate of the average exponent confirms “ $-3$ ” low frequency slope caused by IGWs in turbulent spectra, which were observed in the 300 m lower layer of the SBL [43].

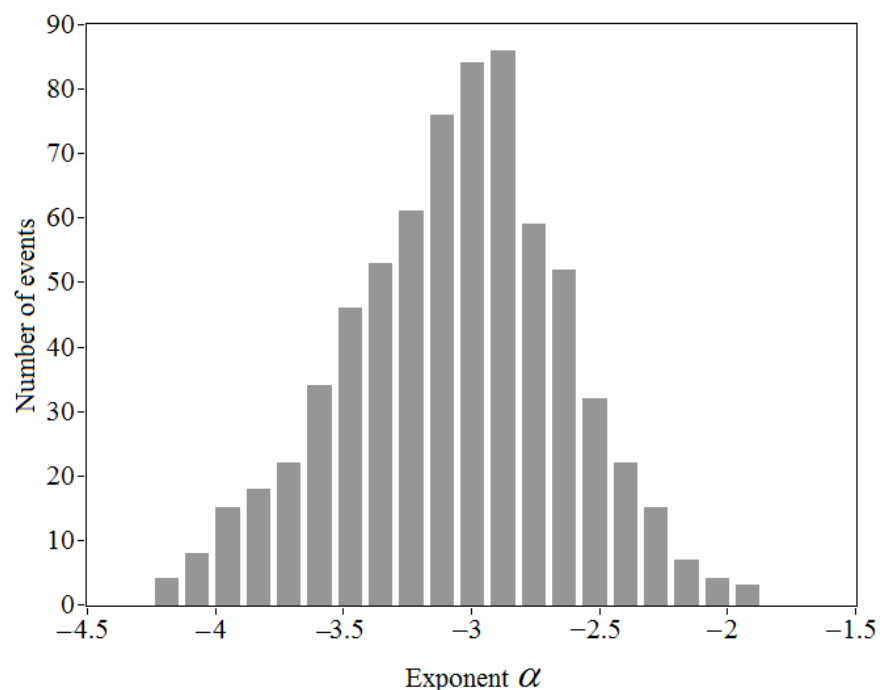


**Figure 13.** A histogram of the exponent  $\alpha$  of the spectrum of vertical wind velocity in the low-frequency range during IGW propagation in the stable atmospheric boundary layer.

We believe that in accordance with the terminology [55], we observed buoyancy IGWs that appear much less often than Kelvin–Helmholtz [44] ones. In each specific event of such type of IGW, the low-frequency slope of the turbulent spectrum can significantly deviate from that which is determined by the average exponent  $\langle \alpha \rangle = -3$ . The histogram in Figure 13 gives the values and corresponding probabilities of these deviations.

## 5. Conclusions

The paper presents experimental data and results of the study of wave turbulence interactions in the stable atmospheric boundary layer. The analysis was based on the data of lidar measurements of the vertical component of wind velocity during IGW propagation with the use of temperature data of the microwave radiometer in the spring–summer periods of 2020–2022 in Tomsk, Russia. The results obtained allow us to draw the following conclusions.

In the overwhelming majority of cases, IGWs in a stably stratified boundary layer occur during LLJs. During the measurements, only two cases of IGW formation in the absence of a jet were revealed. This happened when the wind speed did not exceed 3 m/s, and the wind direction alternated sharply to the opposite direction with height. It is possible that the vertical inhomogeneity of the wind in the velocity (LLJ) or in the direction is one of the reasons for IGW generation in the SBL.

With the appearance of the IGW, the amplitude of the spectrum of turbulent fluctuations in the vertical component of the wind velocity increases significantly, sometimes by orders of magnitude, in the vicinity of the frequency of the IGW-induced quasi-harmonic velocity oscillations compared to the spectral amplitudes at these frequencies in the absence of the IGW. This leads to an increase in the variance of fluctuations of the vertical velocity during the IGW, which is the sum of spectral amplitudes in the entire frequency range. IGW energy is transferred to small-scale turbulence. As a result, the slope of the spectrum of vertical velocity in the low-frequency range between the frequency of IGW-induced oscillations and the frequency of the lower boundary of the inertial range exceeds the slope corresponding to the  $-5/3$  power-law frequency dependence of the spectrum. IGW energy is transferred into the inertial interval of turbulence as well. The amplitude of the spectrum in the inertial frequency range may increase by an order of magnitude due to an increase in the TKE dissipation rate during the IGW.

A total of 700 spectral estimates obtained in the measurements show that during the IGW, the spectra of the vertical velocity in the low-frequency range between the frequency of IGW-induced oscillations and the frequency of the lower boundary of the inertial range obey the power-law frequency dependence, with the exponent  $\alpha$  ranging from  $-4.2$  to  $-1.9$ . Eighty percent of  $\alpha$  estimates fall within the range from  $-3.5$  to  $-2.5$ . The average value of the exponent is  $\langle \alpha \rangle = -3$ , which is consistent with a low-frequency slope caused by IGWs in turbulent spectra in a lower layer of the SBL. We believe that in this study, we observed buoyancy IGWs that appear not often. In each specific event of such type of IGW, the low-frequency slope of the turbulent spectrum can significantly deviate from that which is determined by the average exponent  $\langle \alpha \rangle = -3$ . The accumulated database of the exponent of the spectra power-law frequency dependencies gives the values and corresponding probabilities of these deviations.

**Author Contributions:** Conceptualization, V.A.B.; methodology, V.A.B. and I.N.S.; software, I.N.S.; experiment, V.A.B.; validation, I.N.S.; investigation, V.A.B. and I.N.S.; writing—original draft preparation, V.A.B. and I.N.S.; writing—review and editing, V.A.B.; visualization, I.N.S.; supervision, V.A.B.; project administration, V.A.B.; funding acquisition, V.A.B. All authors have read and agreed to the published version of the manuscript.

**Funding:** The work was performed under the project of the Russian Science Foundation 19-17-00170-P. The use of the infrastructure of BEO and developing the algorithm for calculating the error of the lidar estimate of the turbulence energy dissipation rate was supported by the Ministry of Science and Higher Education of the Russian Federation (V.E. Zuev Institute of Atmospheric Optics of Siberian Branch of the Russian Academy of Sciences).

**Data Availability Statement:** The data presented in this study are available from the authors upon request.

**Acknowledgments:** The authors are grateful to our colleagues A.V. Falits and A.M. Sherstobitov for their help in conducting the lidar experiment and processing the experimental data.

**Conflicts of Interest:** The authors declare no conflict of interest. The funders had no role in the design of the study; in the collection, analyses, or interpretation of data; in the writing of the manuscript, and in the decision to publish the results.

## References

1. Lumley, J.L.; Panofsky, H.A. *The Structure of Atmospheric Turbulence*; Interscience Publishers: New York, NY, USA, 1964.
2. Monin, A.S.; Yaglom, A.M. *Statistical Fluid Mechanics, Volume II: Mechanics of Turbulence*; M.I.T. Press: Cambridge, MA, USA, 1971.
3. Zilitinkevich, S.S. *Dynamics of Atmospheric Boundary Layer*; Gidrometeoizdat: Leningrad, Russia, 1970; p. 292. (In Russian)
4. Laikhtman, D.L. *Physics of Atmospheric Boundary Layer*; Gidrometeoizdat: Leningrad, Russia, 1970; p. 342.
5. Vinnichenko, N.K.; Pinus, N.Z.; Shmeter, R.M.; Shur, G.N. *Turbulence in the Free Atmosphere*; Springer Science+Business Media: New York, NY, USA, 1980.
6. Nieuwstadt, F.T.M.; Van Dop, H. *Atmospheric Turbulence and Air Pollution Modelling*; A Course Held in the Hague, 21–25 September, 1981; Springer: Berlin/Heidelberg, Germany, 1982; p. 351.
7. Grachev, A.A.; Andreas, E.L.; Fairall, C.W.; Guest, P.S.; Persson, P.O.G. The critical Richardson number and limits of applicability of local similarity theory in the stable boundary layer. *Bound.-Layer Meteorol.* **2013**, *147*, 51–82. [\[CrossRef\]](#)
8. Zilitinkevich, S.S. *Atmospheric Turbulence and Planetary Boundary Layers*; Fizmatlit: Moscow, Russia, 2013; ISBN 978-5-9221-1519-3. (In Russian)
9. Byzova, N.L.; Ivanov, V.N.; Garger, E.K. *Turbulence in Atmospheric Boundary Layer*; Gidrometeoizdat: Leningrad, Russia, 1989; p. 263. (In Russian)
10. Banta, R.M.; Newsom, R.K.; Lundquist, J.K.; Pichugina, Y.L.; Coulter, R.L.; Mahrt, L. Nocturnal low-level jet characteristics over Kansas during CASES-99. *Bound.-Layer Meteorol.* **2002**, *105*, 221–252. [\[CrossRef\]](#)
11. Edwards, J.M.; Beljaars, A.C.M.; Holstag, A.A.M.; Lock, A.P. Representation of boundary-layer processes in numerical weather prediction and climate models. *Bound.-Layer Meteorol.* **2020**, *177*, 511–539. [\[CrossRef\]](#)
12. Sun, J.; Nappo, C.J.; Mahrt, L.; Belušić, D.; Grisogono, B.; Stauffer, D.R.; Pulido, M.; Staquet, C.; Jiang, Q.; Pouquet, A.; et al. Review of wave turbulence interactions in the stable atmospheric boundary layer. *Rev. Geophys.* **2015**, *53*, 956–993. [\[CrossRef\]](#)
13. Kolmogorov, A.N. Local structure of turbulence in incompressible viscous fluid at very large Reynolds numbers. *Dokl. Akad. Nauk. SSSR* **1941**, *30*, 299–303. (In Russian)
14. Obukhov, A.M. On the distribution of energy in the spectrum of turbulent flow. *Izv. Ross. Akad. Nauk. Seriya Geogr.* **1941**, *5*, 453–463. (In Russian)
15. Lamley, J.P. The spectrum of nearly inertial turbulence in a stably stratified fluid. *J. Atmos. Sci.* **1964**, *21*, 99–102. [\[CrossRef\]](#)
16. Bolgiano, R.J. Structure of turbulence in stratified media. *J. Geophys. Res.* **1962**, *67*, 3015–3023. [\[CrossRef\]](#)
17. Monin, A.S. Spectrum of turbulence in a thermally inhomogeneous atmosphere. *Izv. Ross. Akad. Nauk. Seriya Geogr.* **1962**, *3*, 397–407. (In Russian)
18. Shur, G.N. Experimental investigations of energy spectrum of atmospheric turbulence. *Tr. TsAO* **1962**, *43*, 79–91. (In Russian)
19. Dewan, E.M. Stratospheric wave spectra resembling turbulence. *Science* **1979**, *204*, 832–835. [\[CrossRef\]](#) [\[PubMed\]](#)
20. Nastrom, G.D.; Gage, K.S. A climatology of atmospheric wavenumber spectra of wind and temperature observed by commercial aircraft. *J. Atmos. Sci.* **1985**, *42*, 950–960. [\[CrossRef\]](#)
21. Hostetler, C.A.; Gardner, C.S. Observations of horizontal and vertical wave number spectra of gravity wave motions in the stratosphere and mesosphere over the mid-Pacific. *J. Geophys. Res.* **1994**, *99*, 1283–1302. [\[CrossRef\]](#)
22. Bacmeister, J.T.; Eckermann, S.D.; Newman, P.A.; Lait, L.; Chan, K.R.; Loewenstein, M.; Proffitt, M.H.; Gary, B.L. Stratospheric horizontal wavenumber spectra of winds, potential temperature, and atmospheric tracers observed by high-altitude aircraft. *J. Geophys. Res.* **1996**, *101*, 9441–9470. [\[CrossRef\]](#)
23. Dewan, E.M. Saturated cascade similitude theory of gravity wave spectra. *J. Geophys. Res.* **1997**, *102*, 29799–29817. [\[CrossRef\]](#)
24. Lindborg, E. The energy cascade in a strongly stratified fluid. *J. Fluid Mech.* **2006**, *550*, 207–242. [\[CrossRef\]](#)
25. Lindborg, E. Horizontal wavenumber spectra of vertical vorticity and horizontal divergence in the upper troposphere and lower stratosphere. *J. Atmos. Sci.* **2007**, *64*, 1017–1025. [\[CrossRef\]](#)
26. Skamarock, W.C.; Park, S.H.; Klemp, J.B.; Snyder, C. Atmospheric kinetic energy spectra from global high-resolution nonhydrostatic simulations. *J. Atmos. Sci.* **2014**, *71*, 4369–4381. [\[CrossRef\]](#)
27. Callies, J.; Ferrari, R.; Bühler, O. Transition from geostrophic turbulence to inertia-gravity waves in the atmospheric energy spectrum. *Proc. Natl. Acad. Sci. USA* **2014**, *111*, 17033–17038. [\[CrossRef\]](#)
28. Lindborg, E. A Helmholtz decomposition of structure functions and spectra calculated from aircraft data. *J. Fluid Mech.* **2015**, *762*, R4. [\[CrossRef\]](#)
29. Chunchuzov, I.P. Nonlinear formation of the three-dimensional spectrum of mesoscale wind velocity and temperature fluctuations in a stably stratified atmosphere. *J. Atmos. Sci.* **2018**, *75*, 3447–3467. [\[CrossRef\]](#)
30. Kan, V.; Gorbunov, M.E.; Sofieva, V.F. Fluctuations of radio occultation signals in sounding the Earth's atmosphere. *Atmos. Meas. Tech.* **2018**, *11*, 663–680. [\[CrossRef\]](#)
31. Kan, V.; Gorbunov, M.E.; Shmakov, A.V.; Sofieva, V.F. Reconstruction of the internal-wave parameters in the atmosphere from signal amplitude fluctuations in a radio-occultation experiment. *Izv. Atmos. Ocean. Phys.* **2020**, *56*, 435–447. [\[CrossRef\]](#)
32. Lilly, D.K.; Lester, P.F. Waves and turbulence in the stratosphere. *J. Atmos. Sci.* **1974**, *31*, 800–812. [\[CrossRef\]](#)



33. Hertzog, A.; Vial, F.; Mechoso, C.R.; Basdevant, C.; Cocquerez, P. Quasi-Lagrangian measurements in the lower stratosphere reveal an energy peak associated with near-inertial waves. *Geophys. Res. Lett.* **2002**, *29*, 1229. [\[CrossRef\]](#)
34. Gurvich, A.S.; Chunchuzov, I.P. Three-dimensional spectrum of temperature fluctuations in stably stratified atmosphere. *Ann. Geophys.* **2008**, *26*, 2037–2042. [\[CrossRef\]](#)
35. Nastrom, G.D.; Fritts, D.C.; Gage, K.S. An investigation of terrain effects on the mesoscale spectrum of atmospheric motions. *J. Atmos. Sci.* **1987**, *44*, 3087–3096. [\[CrossRef\]](#)
36. Mahrt, L.; Gamage, N. Observations of turbulence in stratified flow. *J. Atmos. Sci.* **1987**, *44*, 1106–1121. [\[CrossRef\]](#)
37. Guo, Y.; Liu, A.Z.; Gardner, C.S. First Na lidar measurements of turbulence heat flux, thermal diffusivity, and energy dissipation rate in the mesopause region. *Geophys. Res. Lett.* **2017**, *44*, 5782–5790. [\[CrossRef\]](#)
38. Vincent, R.A.; Allen, S.J.; Eckermann, S.D. Gravity wave parameters in the lower stratosphere. In *Gravity Wave Processes: Their Parameterization in Global Climate Models*; Hamilton, K., Ed.; NATO ASI Series; Springer-Verlag: Berlin, Germany, 1997; pp. 7–25.
39. Fritts, D.C.; Alexander, M.J. Gravity wave dynamics and effects in the middle atmosphere. *Rev. Geophys.* **2003**, *41*, 1003. [\[CrossRef\]](#)
40. Gurvich, A.S.; Chunchuzov, I.P. Parameters of the fine density structure in the stratosphere obtained from spacecraft observations of stellar scintillations. *J. Geophys. Res.* **2003**, *108*, 4166. [\[CrossRef\]](#)
41. Tsuda, T. Characteristics of atmospheric gravity waves observed using the MU (middle and upper atmosphere) radar and GPS (global positioning system) radio occultation. *Proc. Japan Acad.* **2014**, *90B*, 12–27. [\[CrossRef\]](#) [\[PubMed\]](#)
42. Zhang, S.D.; Huang, C.M.; Huang, K.M.; Gong, Y.; Chen, G.; Gan, Q.; Zhang, Y.H. Latitudinal and seasonal variations of vertical wave number spectra of three-dimensional winds revealed by radiosonde observations. *J. Geophys. Res. Atmos.* **2017**, *122*, 13–174. [\[CrossRef\]](#)
43. Finnigan, J.J.; Einaudi, F.; Fua, D. The interaction between an internal gravity wave and turbulence in the stably-stratified nocturnal boundary layer. *J. Atmos. Sci.* **1984**, *41*, 2409–2436. [\[CrossRef\]](#)
44. Stull, R.B. *An Introduction to Boundary Layer Meteorology*; Kluwer Academic Publishers: Dordrecht, The Netherlands; Boston, MA, USA; London, UK, 1988; ISBN 90-277-2768-6.
45. Pearson, G.; Davies, F.; Collier, C. An analysis of performance of the UFAM Pulsed Doppler lidar for the observing the boundary layer. *J. Atmos. Ocean. Technol.* **2009**, *26*, 240–250. [\[CrossRef\]](#)
46. Banakh, V.A.; Smalikho, I.N.; Falits, A.V.; Sherstobitov, A.M. Estimating the parameters of wind turbulence from spectra of radial velocity measured by a pulsed Doppler lidar. *Remote Sens.* **2021**, *13*, 2071. [\[CrossRef\]](#)
47. Smalikho, I.N.; Banakh, V.A. Effect of wind transport of turbulent inhomogeneities on estimation of the turbulence energy dissipation rate from measurements by a conically scanning coherent Doppler lidar. *Remote Sens.* **2020**, *12*, 2802. [\[CrossRef\]](#)
48. Banakh, V.A.; Smalikho, I.N. Lidar observations of atmospheric internal waves in the boundary layer of atmosphere on the coast of Lake Baikal. *Atmos. Meas. Tech.* **2016**, *9*, 5239–5248. [\[CrossRef\]](#)
49. Banakh, V.A.; Smalikho, I.N. *Coherent Doppler Wind Lidars in a Turbulent Atmosphere*; Artech House: Boston, MA, USA; London, UK, 2013; p. 248. ISBN 978-1-60807-667-3.
50. Taylor, G.I. The spectrum of turbulence. *Proc. R. Soc. London. Ser. A-Math. Phys. Sci.* **1938**, *164*, 476–490. [\[CrossRef\]](#)
51. Smalikho, I.N.; Banakh, V.A. Measurements of wind turbulence parameters by a conically scanning coherent Doppler lidar in the atmospheric boundary layer. *Atmos. Meas. Tech.* **2017**, *10*, 4191–4208. [\[CrossRef\]](#)
52. Banakh, V.A.; Smalikho, I.N.; Falits, A.V. Estimation of the turbulence energy dissipation rate in the atmospheric boundary layer from measurements of the radial wind velocity by micropulse coherent Doppler lidar. *Opt. Expr.* **2017**, *25*, 22679–22692. [\[CrossRef\]](#)
53. Kadygrov, E.N. Microwave radiometry of atmospheric boundary layer: Method, equipment, and applications. *Opt. Atmos. i Okeana* **2009**, *22*, 697–704. (In Russian)
54. Banakh, V.A.; Smalikho, I.N.; Falits, A.V. Wind-Temperature Regime and Wind Turbulence in a Stable Boundary Layer of the Atmosphere: Case Study. *Remote Sens.* **2020**, *12*, 955. [\[CrossRef\]](#)
55. Zaytseva, D.; Kallistratova, M.; Lyulyukin, V.; Kouznetsov, R.; Kuznetsov, D. On the influence of internal gravity waves on the intensity of turbulence in the atmospheric boundary layer. *IOP Conf. Series Earth Environ. Sci.* **2022**, *1040*, 012034. [\[CrossRef\]](#)

**Disclaimer/Publisher's Note:** The statements, opinions and data contained in all publications are solely those of the individual author(s) and contributor(s) and not of MDPI and/or the editor(s). MDPI and/or the editor(s) disclaim responsibility for any injury to people or property resulting from any ideas, methods, instructions or products referred to in the content.